Composites Part B 277 (2024) 111368

Contents lists available at ScienceDirect

Composites Part B

journal homepage: www.elsevier.com/locate/compositesb

"Subconsciousness-triggered" human body defensive strategy: Bi-stability intelligent joint with bionic kirigami structure

Jianyu Zhou [a], Mei Liu [b], Sheng Wang [a,**], Junshuo Zhang [a], Mingyang Ni [a], Shuai Liu [a], Yu Wang [a], Huaxia Deng [a], Bing Liu [a], Xinglong Gong [a,c,*]

[a] CAS Key Laboratory of Mechanical Behavior and Design of Materials, Department of Modern Mechanics, University of Science and Technology of China, Hefei, Anhui, 230027, PR China

[b] Equine Science Research and Doping Control Center, School of Physical Education, Wuhan Business University, Wuhan, Hubei, 430056, PR China

[c] State Key Laboratory of Fire Science, University of Science and Technology of China, 96 Jinzhai Road, Hefei, Anhui, 230026, PR China

ARTICLE INFO

Handling editor: Hao Wang

Keywords:
A
Aramid fibre A
Fabrics/textiles A
Smart materials B
Impact behaviour

ABSTRACT

Kirigami structures are increasingly popular in wearable devices due to their exceptional properties. However, their mechanical robustness and anti-impact properties during structural deformation have been overlooked. This study addresses this issue by introducing defects on the surface of composites, mimicking pangolin scales to produce negative Poisson's ratio deformation during tensile strain. Kevlar, conductive shear stiffening elastomer (c-SSE), and PET are combined (Kiri-Kevlar). When subjected to impact, the subconscious rapid response of humans leads to bending arms or curling up, causing Kiri-Kevlar assembled at joints to stretch and undergo structural deformation. The Kiri-Kevlar deformation and high energy dissipation characteristics of c-SSE effectively resist external impact. In summary, a functional-integrated wearable device is developed based on a bionic kirigami structure, realizing efficient anti-impact and providing ideas for a new generation of human-computer interactive intelligent protection devices.

1. Introduction

Kirigami is an ancient art that creates fascinating ornaments by artfully cutting and manipulating a piece of paper. Currently, this art form has evolved into a framework for design and manufacturing [1,2] that enables the creation of multifunctional materials and structures at different scales [3–5]. By skillfully designing geometric slits, simple 2D thin plates can be transformed into complex 3D structures with unique and programmable mechanical properties under external stimulation, such as flexibility [6], super-shape deformation [7], and adjustable Poisson's ratio [8]. Structural design based on kirigami beyond traditional materials has a wide range of potential applications in robotics [9], metamaterials [10], green energy [11], biomedicine [12] and other fields.

The development of wearable devices needs to consider the optimal selection and design of materials and structures for functioning at curvilinear and dynamic surfaces of the human body [13,14]. The structural flexibility of kirigami provides a rich solution to this problem. Gao et al. developed a wearable biosensor inspired by fish scale patterns and kirigami, which confers many advantages, including high stretch ability, breathability, and the capacity to collect sweat for diagnostic and motion monitoring [15]. Phillip Won et al. assembled stretchable electronics with multivariable configurability by cutting highly conductive and transparent electrodes into diverse geometric patterns, based on which they developed an ultra-scalable transparent kirigami heater for personal thermal management [16]. Overall, the flexible and stretchable nature of the kirigami-based structures allows them to conform well to the curved structure of muscle tissue during human movement and adapt to dynamic behaviors.

Nevertheless, many kirigami-based wearables overlook the importance of dynamic mechanical property design, and research on the response of mechanical properties under dynamic impact loading is scarce. As people's security awareness continues to increase, the demand for wearable devices that can protect users under extreme impact becomes more urgent [17–19]. In fact, certain kirigami structures possess great potential in the field of impact resistance due to their

* Corresponding author. CAS Key Laboratory of Mechanical Behavior and Design of Materials, Department of Modern Mechanics, University of Science and Technology of China, Hefei, Anhui, 230027, PR China.

** Corresponding author.

E-mail addresses: wsh160@ustc.edu.cn (S. Wang), gongxl@ustc.edu.cn (X. Gong).

https://doi.org/10.1016/j.compositesb.2024.111368

Received 17 December 2023; Received in revised form 5 March 2024; Accepted 7 March 2024

Available online 16 March 2024

auxeticity or ability to form load-bearing structures [20]. Li et al. proposed a novel kirigami corrugated structure that incorporates additional vertical breaking resistance and restraint between structural planes. In comparison to traditional corrugated structures, the deformation behavior of the kirigami corrugated structure undergoes significant changes under out-of-plane crushing, resulting in a substantial improvement in energy absorption [21,22]. Chan-Young Park et al. proposed a kirigami and origami-based structure to study the impact of hollow patterns on aerodynamics, which can cushion against collisions and falls, protecting drones from damage [23]. The researches demonstrate that kirigami structures are excellent candidates for anti-impact design. However, the kirigami structures currently employed in the field of anti-impact are often structurally heavy and rigid, which is contrary to the requirements of flexibility and adaptability in wearable device design. When designing flexible anti-impact devices, the selection of materials is crucial. In recent years, researchers have shown significant interest in the unique shear stiffening effect exhibited by some new smart materials. The shear stiffening elastomers (SSE) have become widely popular for use in wearable protective devices due to their exceptional cushioning and energy dissipation properties during impacts [24,25]. It is also noteworthy that SSE, as an excellent polymer matrix, can be combined with various functional materials to achieve conductivity, thereby laying the groundwork for developments in human-computer interaction and other related fields.

In this work, inspired by the scales of the pangolin, a flexible composite is developed by combining Kevlar, shear c-SSE, and PET, utilizing the kirigami structure (Kiri-Kevlar). Kiri-Kevlar exhibits excellent mechanical properties and can seamlessly transition between 2D and 3D modes. Due to the structural stiffness of Kiri-Kevlar itself and the unique strain-rate-sensitive properties of c-SSE, it has demonstrated an extraordinary ability to dissipate impact forces, even withstanding the impact of high-speed bullets. Moreover, Kiri-Kevlar can be comfortably worn on curved areas of the human body, remaining flat when relaxed. When subjected to impact, the subconscious actions of the body, such as curling up or bending limbs, trigger the activation of the kirigami structure of Kiri-Kevlar, effectively acting as an impact buffer. Additionally, Kiri-Kevlar enables intelligent human-computer interaction based on its electrical properties. By wearing Kiri-Kevlar, users can control computer games through multiple channels.

2. Materials and methods

2.1. Materials

Hydroxyl silicone oil was provided by Guangzhou Gongwang New Material Technology Co., LTD. Boric acid, octanoic acid, hydroiodic acid and ethanol were supplied by Sinopharm Chemical Reagent Co., Ltd, Shanghai, China. Carbon nanotubes (CNTs) were supplied by Suzhou Carbon Feng Graphene Technology Co., LTD. PET film was purchased from Wuxi Xiaguang Plastic Industry Technology Co., LTD. The fabric used in this work was the plain-woven aramid Kevlar fabric 129 with an areal density of 200 g/m^2 (tensile strength: 3.45 GPa; elongation at break: 3.4%; initial modulus: 97 GPa). It was also commercially available.

2.2. Preparation of conductive shear stiffening gel (c-SSG)

To prepare c-SSG, hydroxy silicone oil and boric acid were mixed in a mass ratio of 30:1. A corresponding mass fraction of CNTs was added to the mixture, which was then heated at 180 °C. The mixture was stirred every 15 min until it completely congealed into lumps. Subsequently, 250 μL of octanoic acid was added per 100 g of hydroxy silicone oil, and the mixture was stirred thoroughly again. After heating for 30 min, c-SSG was successfully synthesized.

2.3. Fabrication of Kevlar-based composite with kirigami structure (Kiri-Kevlar)

To prepare Kiri-Kevlar with structural deformation ability, it was necessary to first create periodic notches on a PET film using laser engraving. A mixture of c-SSG and VMQ in a 7:3 mass ratio, along with a 4% mass fraction of benzoyl peroxide, was then laid on the PET film in a mold, followed by a layer of Kevlar fabric on top. The entire mixture in the mold was then hot pressed at 100 °C and 20 MPa for 30 min, allowing the c-SSG and VMQ to vulcanize to c-SSE. Finally, a hand cutter was used to create a notch in the composite material along the preexisting notch in the PET film, resulting in the successful preparation of Kiri-Kevlar with an adjustable structure.

2.4. Characterization

The microstructures of the materials were characterized by SEM (Gemini SEM 500, ZEISS) equipped with an energy-dispersive spectroscopy (EDS) system. The rheological properties of the polymer matrix were measured by a commercial rheometer (Physica MCR 301, Anton Paar Co., Austria). Fourier transform infrared spectra were obtained using an FTIR Nicolet 8700 (Thermo Nicolet, USA). The uniaxial tensile, structured Kiri-Kevlar compression and peeling test was conducted with a universal testing machine (MTS Criterion™ Model 43). The force dissipation property of Kiri-Kevlar was studied by a low-velocity impact drop tower testing system consisting of a drop tower test device (ZCJ1302-A, MTS Co. Ltd, China), acceleration sensor and force sensors. The high-speed impact system consisted of an air gun and a laser velocimeter, which controlled the initial velocity of the bullet by controlling the initial air pressure of the air gun, and the initial velocity could be collected through the laser velocimeter. A high-speed camera (Phantom V2512) was set up behind the sample to record the impact at different speeds. The water contact angle was measured by a contact angle measuring instrument (JY-82C, Chengde Dingsheng Co., LTD, China). The electrical properties of the materials were measured by the Modu-Lab Materials Test System (Solartron Analytical, AMETEK Advanced Measurement Technology, Inc., United Kingdom). The Kiri-Kevlar was connected to a voltage divider circuit to control the computer by electrical signals. The signal acquisition system (USB3136, Altai Technology Development Co., LTD, China) transmitted these electrical signal data to the computer for processing, which was carried out using the LabView program.

3. Results and discussion

3.1. Design and fabrication of bionic kirigami structure Kevlar (Kiri-Kevlar) composite

The pangolin is a remarkable example of nature's ability to create stretchable and impact-resistant structures [26,27]. Its body is covered in overlapping scales that provide both flexibility and protection against predators (Fig. 1a). When threatened, the pangolin will assume a curled posture. Due to the tensile stress on the outer surfaces during the bending process (Fig. 1b), the scales will extend outward, creating a half-opened pine cone shape. It is evident that periodic intervals and defects between scales can induce structural modifications. For the bionic design of such structures, laser engraving is employed to etch lines on PET film (Fig. 1c, Figure S1). This method is versatile and can be applied to process a diverse range of kirigami structures (Figure S2). Subsequently, Kevlar, c-SSG, and PET are integrated using the hot-pressing method while also creating a corresponding notch (Fig. 1d). During the hot-pressing process, the molecular chains in the c-SSG containing BPO are cross-linked and vulcanized to produce c-SSE (Fig. 1e). Fig. 1f displays the infrared spectra of VMQ, SSE, and c-SSE. As silicon-based materials, these three substances exhibit typical *Si*-O bands at 1008 cm^{-1}. Notably, the addition of boric acid to SSE and c-SSE

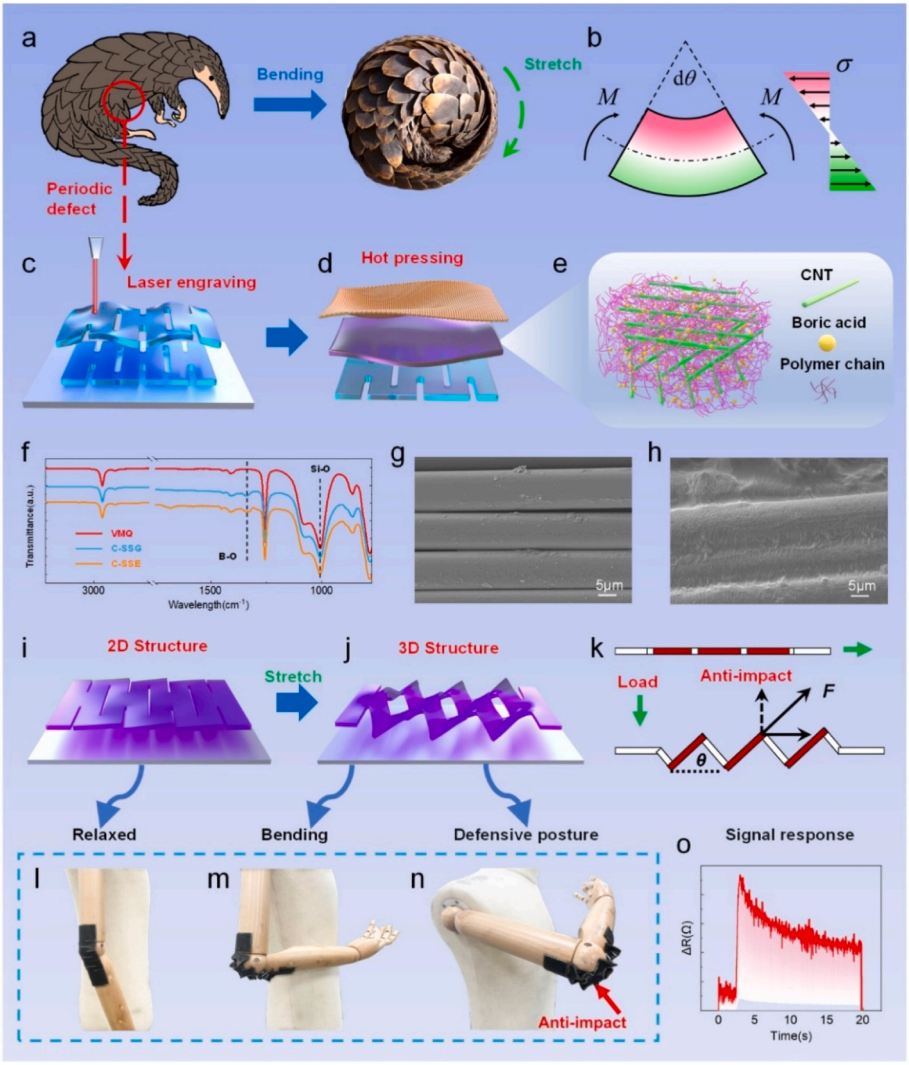

Fig. 1. (a) Schematic diagram of a pangolin curling up and raising its scales; (b) stress distribution in the direction of thickness of bending element; (c–e) preparation process diagram of Kiri-Kevlar; (f) infrared spectra of VMQ, c-SSG and c-SSE; SEM images of Kevlar surface (g) before and (h) after hot pressing; (i, j) schematic diagrams of structural change of Kiri-Kevlar caused by stretching; (k) simplified deformation model of Kiri-Kevlar; (l) when the Kiri-Kevlar is worn on the joints, (m, n) it opened the bionic scales with the bending of the arm for anti-impact; (o) Kiri-Kevlar also had sensitive sensing capability during impact.

results in a characteristic peak at 1340 cm^{-1}, which represents the "B-O" dynamic bond characteristic peak [28]. Neat Kevlar exhibits a smooth surface with weak interfiber bonding (Fig. 1g). Upon hot pressing, a portion of c-SSE adheres to the fiber surface (Fig. 1h), with a more pronounced effect at the intersection of warp and weft fiber bundles (Figure S3a). The side view of Kiri-Kevlar reveals that c-SSE acts as an intermediate layer, firmly bonding the PET film to Kevlar fabric (Figure S3b). A detailed analysis of the interfacial properties between the materials will be provided in Section 3.5. Kiri-Kevlar undergoes a structural transformation from a 2D to a 3D configuration when subjected to a pre-tensile load, akin to the scales of a pangolin expanding (Fig. 1i and j). Specifically, structureless Kiri-Kevlar is described as Kiri-Kevlar with free boundary condition and two-dimensional state. When subjected to tensile loads and transformed into a three-dimensional structure, it is defined as structured Kiri-Kevlar. Furthermore, the Kiri-Kevlar exhibits flexibility (Figure S4), allowing it to be comfortably contoured and worn on the human body. As a result of prestrain-induced structural deformation, the structured Kiri-Kevlar provides support when impacted, allowing deformation and resisting the impact energy (Fig. 1k). According to Figure S5, the human body responds to falls and impact in various ways by instinctively assuming a protective posture [29–31]. Curling up, which is a form of pre-strain, can initiate the deformation of the Kiri-Kevlar. For example, when worn over human joint areas, Kiri-Kevlar initially assumes a flat state during the arm hangs in a natural position (Fig. 1l). In the event of a fall or external impact, the subconscious reaction of the individual prompts them to quickly bend their arms to assume a defensive posture and resist the impact (Fig. 1m and n). Fortunately, Kiri-Kevlar's structure deforms in tandem with the arm's movement, providing an immediate increase in impact resistance. Kiri-Kevlar can also generate corresponding resistance signals with various deformation modes, thus providing a foundation for the development of intelligent sensing, human-computer interaction, and other related functions (Fig. 1o).

3.2. *Rheological and electrical properties of unstructured Kiri-Kevlar composites*

Prior to investigating the properties of structured Kiri-Kevlar, it is essential to study the unstructured composite itself. It is worth noting that the anti-impact properties of Kiri-Kevlar are partly attributed to the rheological properties of c-SSE in conjunction with Kevlar. As the raw material for c-SSE, the storage modulus (G') of c-SSG exhibits significantly increase with increasing loading frequency (Fig. 2a). Meanwhile, the loss modulus (G'') initially increases before eventually decreasing

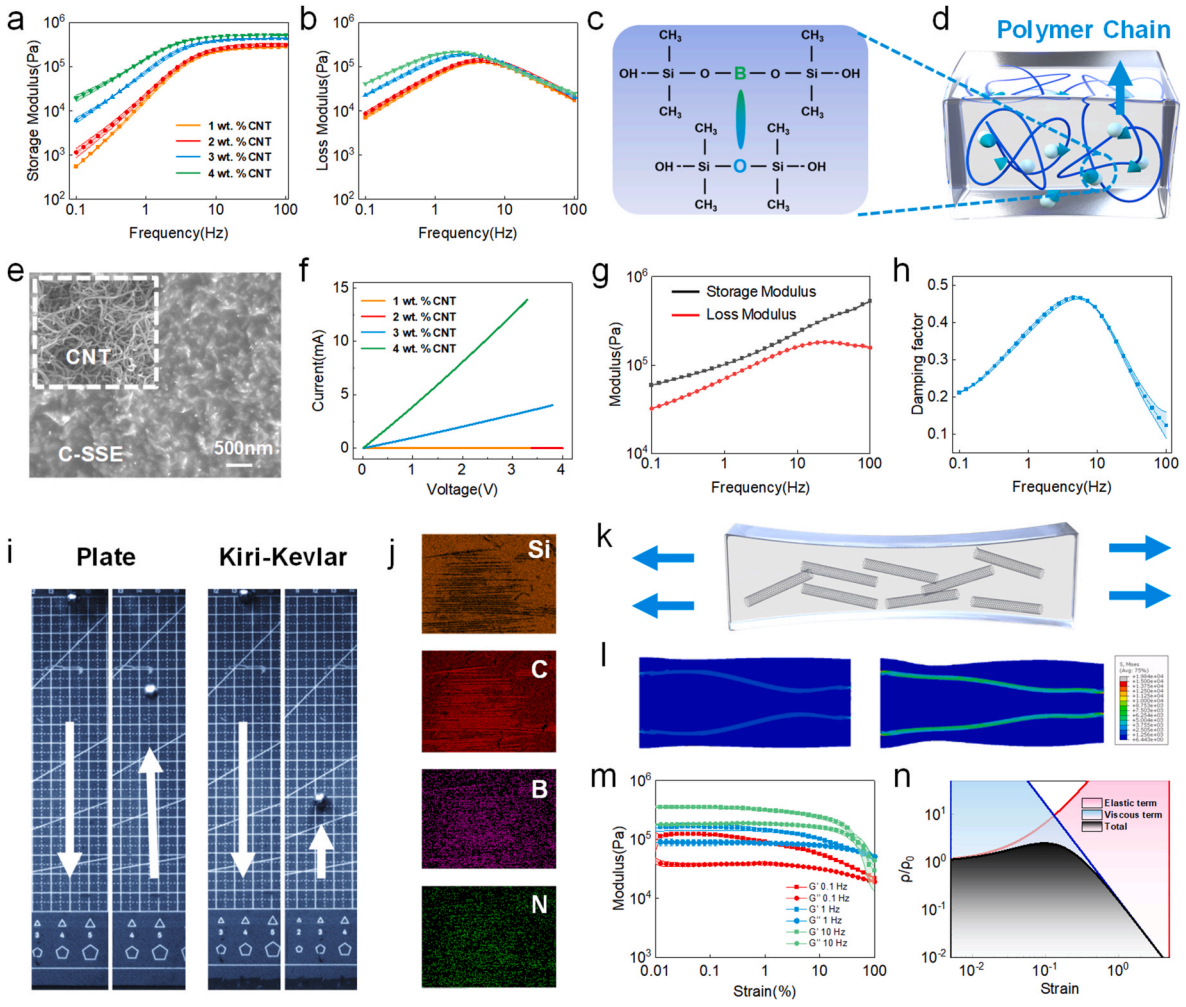

Fig. 2. Sweep-frequency (a) storage modulus and (b) loss modulus of c-SSG with different mass fractions of CNTs; (c) structure of boron-oxygen bond in (d) c-SSE after vulcanization; (e) SEM images of CNTs and c-SSE; (f) stable I-V curves of c-SSG with different mass fractions of CNTs; sweep-frequency (g) storage modulus, loss modulus and (h) damping factor of Kiri-Kevlar; (i) height comparison of ball rebounding after falling on Kiri-Kevlar and rigid plate; (j) EDS elemental mapping images of Kiri-Kevlar surface; (k) schematic diagram of conductive path changing during matrix deformation; (l) FEM simulation result of embedded CNTs in polymer under tensile loading; (m) sweep-strain storage modulus and loss modulus of Kiri-Kevlar under different frequencies; (n) elastic term and the viscous term of relative resistance change.

(Fig. 2b). The addition of CNTs greatly enhances the initial modulus and overcomes the cold flow behavior of pure shear stiffening gel (SSG) (Figure S6). The typical strain-rate effect is attributed to the presence of dynamic "B-O″ bonds in the polymer chain (Fig. 2c). At high strain rates, these bonds (Fig. 2d) do not have sufficient time to separate, thereby elevating the macrolevel modulus of SSG. The SEM images clearly demonstrate the uniform dispersion of CNTs within the SSG (Fig. 2e). At a CNTs mass fraction of 3%, the seepage threshold is reached, resulting in a significant enhancement of the conductivity of c-SSG (Fig. 2f). Consequently, c-SSG comprising 3% CNTs is chosen for vulcanization. The strain-scanning shear loading of 3 wt % c-SSG did not reveal an obvious yield point due to its fluid-like nature (Figure S7). Upon being subjected to high temperature and pressure during hot pressing, c-SSG with VMQ undergoes vulcanization and transforms into an elastomer known as c-SSE. The viscoelasticity of vulcanized c-SSE results in a decrease in modulus at high strain (Figure S8). Fig. 2g shows that Kiri-Kevlar exhibits an obvious strain rate effect in the unstructured state, whereas vulcanized VMQ is strain rate independent (Figure S9). The damping factor (ζ) can be calculated by $\zeta = G''/G'$ and reaches a maximum value of 0.47 at a frequency of 5.7 Hz (Fig. 2h). Compared to falling on a rigid plate, Kiri-Kevlar's damping effect dissipates energy and reduces the rebound height of the ball (Fig. 2i–Video S1, S2). The creep and relaxation curves of flat Kiri-Kevlar are shown in Figure S10. C-SSE also carries the electrical conductivity of the Kiri-Kevlar composite. EDS mapping confirms that c-SSE partially penetrates the Kevlar surface (Fig. 2j–S11), resulting in an overall enhancement of the electrical conductivity of the structure. The resistance of a composite material changes as a result of the deformation of the matrix and the alteration of the conductive path formed by CNTs (Fig. 2k). To simulate this process, a CNTs embedded with a polymer model is constructed (Figure S12, Supplementary Discussion 1) [32]. When the polymer is subjected to low strain stimulation, the adjacent CNTs move away from each other, and the overall conductive path becomes elongated, leading to an increase in the overall resistance (Fig. 2l). The yield strain of Kiri-Kevlar is determined to be 6.3% through strain scanning loading tests (Fig. 2m). At higher strains, the number of connections between particles per volume increases linearly with time, resulting in a decrease in resistance (Fig. 2n) [33–35]. This phenomenon can be explained by the effect of elastic and viscous terms (Supplementary Discussion 2).

3.3. Structural evolution of Kiri-Kevlar caused by axial elongation

The deformation process of Kiri-Kevlar's structure under tensile loading requires detailed discussion. The stress–strain curves of Kiri-

Kevlar under different strain rates are shown in Fig. 3a. After undergoing the elastic stage, Kiri-Kevlar's stress–strain curve exhibits a significant reduction in stiffness and eventually fails after reaching the stress limit. Due to the cohesiveness of c-SSE, the failure mode is not a collapse, which is obviously different from single Kevlar and PET. In addition, Kiri-Kevlar demonstrates significant strengthening and toughening under high strain rate loading (Figure S13), which is attributed to the shear stiffening effect. In the elastic range, Kiri-Kevlar shows excellent tensile cycle stability (Fig. 3b). During stretching, the gaps in the structure gradually widen, resulting in the formation of a periodic arch bridge structure (Fig. 3c–Video S3). The twisting of the lateral periodic edges gives rise to a negative Poisson's ratio for the entire structure (Fig. 3d–Video S4). Monolayer Kevlar and PET demonstrate different mechanical behaviors when subjected to tensile loading (Figure S14). Specifically, PET exhibits higher flexural rigidity than Kevlar, rendering it a suitable candidate for use as a stiffness adjustment layer in Kiri-Kevlar [36]. Notably, the primary damage mode in Kevlar is fiber pull-out (Figure S15). To further understand the structural evolution of Kiri-Kevlar during the stretching process, three points (P-up, P-middle, P-down) are identified on the side of one of Kiri-Kevlar's single periodic units (Figure S16a, b). The points P-up and P-down can be traced by fluorescent agent and camera (Figure S17). The acquisition mode of the camera is set to long exposure, and the fluorescence produced by the feature points at different times and in different spatial locations is recorded. The movement of the green points can be considered as the motion trajectory of the feature points during deformation of Kiri-Kevlar. The absolute changes in coordinates for the three points are depicted in Fig. 3e and f. Setting P-middle as the origin, the relative coordinate changes of P-up and P-down relative to P-middle are calculated in a reference coordinate system by Equation (1). The movement of P-up and P-down relative to the midpoint is centrosymmetric (Fig. 3g and h).

$$\begin{cases} \Delta x_{Relative} = \Delta x_{Absolute} - \Delta x_{P-middle} \\ \Delta y_{Relative} = \Delta y_{Absolute} - \Delta y_{P-middle} \end{cases} \quad (1)$$

The structural parameters of Kiri-Kevlar undoubtedly play a pivotal role in determining structural alterations. To investigate the impact of these parameters, finite element models with varying structural characteristics have been constructed (Figure S18a, Table S1). Consistent with the experimental results, three feature points are marked on the

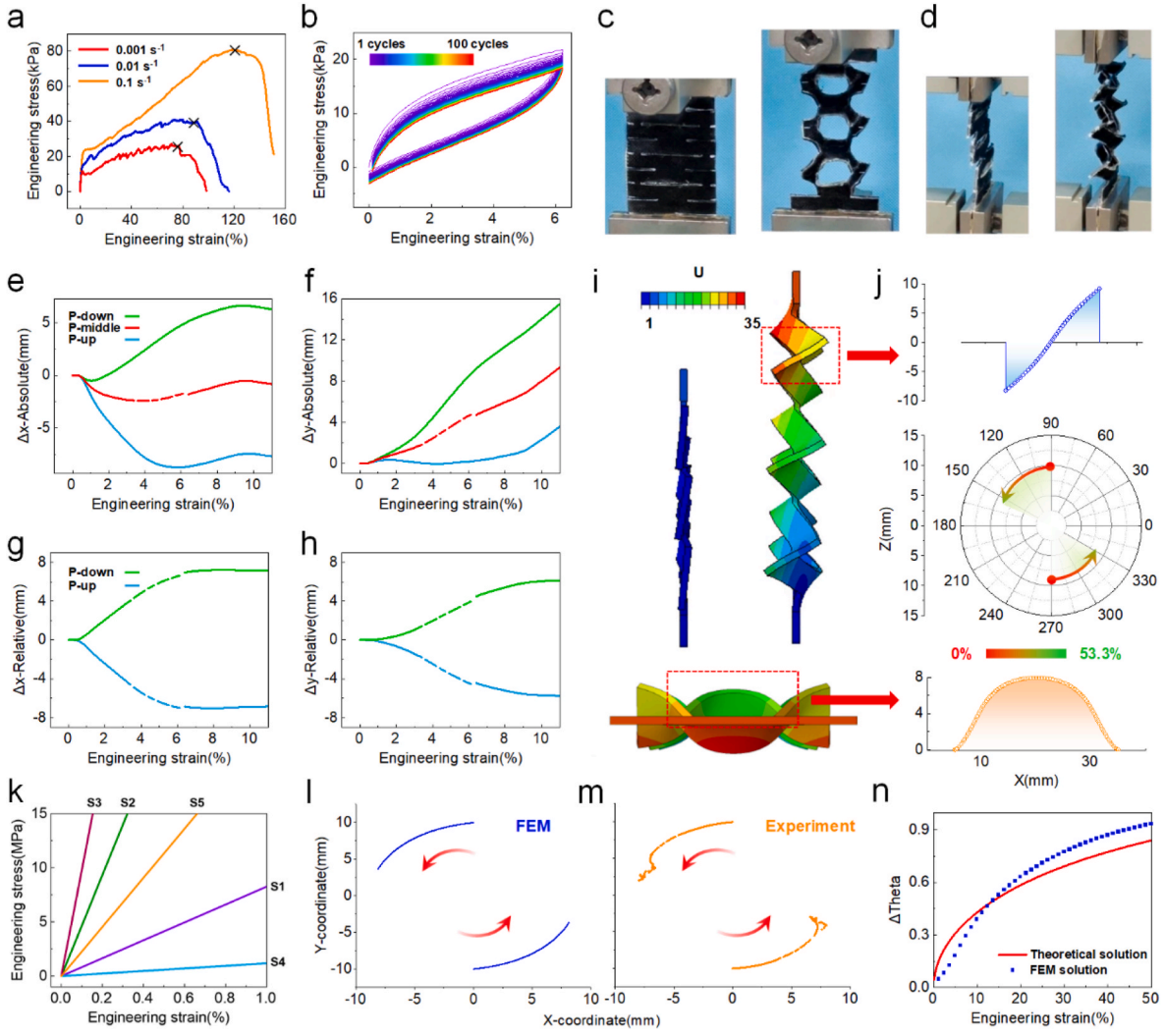

Fig. 3. (a) Typical tensile stress-strain curves of Kiri-Kevlar under different strain rates; (b) tensile properties of Kiri-Kevlar cycling stably within the elastic interval; (c) front view and (d) side view of the structural changes during the Kiri-Kevlar tensile process; change in the X coordinate and Y coordinate of the reference point in the (e, f) absolute coordinate system and (g, h) reference coordinate system based on the midpoint; (i) FEM simulation result of the tensile process of Kiri-Kevlar; (j) characteristic region deformation of Kiri-Kevlar and rotation curve of the reference point in polar coordinates; (k) initial stiffness of Kiri-Kevlar with different structural parameters; (l, m) comparison of reference point coordinate changes in the experiment and FEM simulation; (n) rotation angle of the reference point in polar coordinates as a function of engineering strain.

short edge of the structural unit (Figure S16c, d). By taking the same structural parameters as in the experiment, the FEA simulation result presents structural deformation that agrees with the experiment and allows for characterization of structural parameters that are difficult to measure experimentally (Fig. 3i and j). Furthermore, the deformation of different structural parameters is also considered (Figure S18-S21, Supplementary Discussion 3). Fortunately, the initial stiffness of deformation can be adjusted by structural parameters (Fig. 3k). The trajectory of the FEA feature points relative to the midpoint is compared with the trajectory tracked by the experiment, and the two agree well (Fig. 3l and m). The simplified geometric truss structure of Kiri-Kevlar is shown in Figure S22, and the rotation angle of its feature points under high strain can be predicted by Equation (2) [37].

$$\theta_T = \cos^{-1}\left(\frac{1}{\varepsilon_E + 1}\right) \tag{2}$$

where θ_T and ε_E are the rotation angles calculated by the theoretical model, engineering strain and $\varepsilon_E = \frac{L-L_0}{L_0}$ (Supplementary Discussion 4). The rotation angle calculated by the theoretical model (θ_T) is similar to the angle extracted by the finite element model (θ_F) by Equation (3).

$$\theta_F = \arctan\left|\frac{\Delta y_{Absolute} - \Delta y_{P-middle}}{\Delta x_{Absolute} - \Delta x_{P-middle}}\right| \left(0 \le \theta_F \le \frac{\pi}{2}\right) \tag{3}$$

Under small strains, the angular change caused by the deformation is more pronounced (Fig. 3n). Consequently, when worn on the human body, even a small range of motion can result in significant structural deformation.

3.4. Compression performance of Kiri-Kevlar with varying structural degrees

When Kiri-Kevlar is impacted and provides protection, it is essentially subjected to an out-of-plane compression load with a high strain rate. The Kiri-Kevlar not only provides additional load carrying capacity by the structure, but its modulus span of the shear stiffening effect at high strain rates also collaboratively improves the anti-impact properties [38]. During the compression process of unstructured Kiri-Kevlar, the stress–strain curve exhibits an obvious hysteresis loop due to the viscoelastic property of c-SSE (Fig. 4a). Moreover, the modulus and maximum stress at 10% strain increase significantly with the strain rate (Fig. 4b and c). Cyclic compression experiments are conducted on

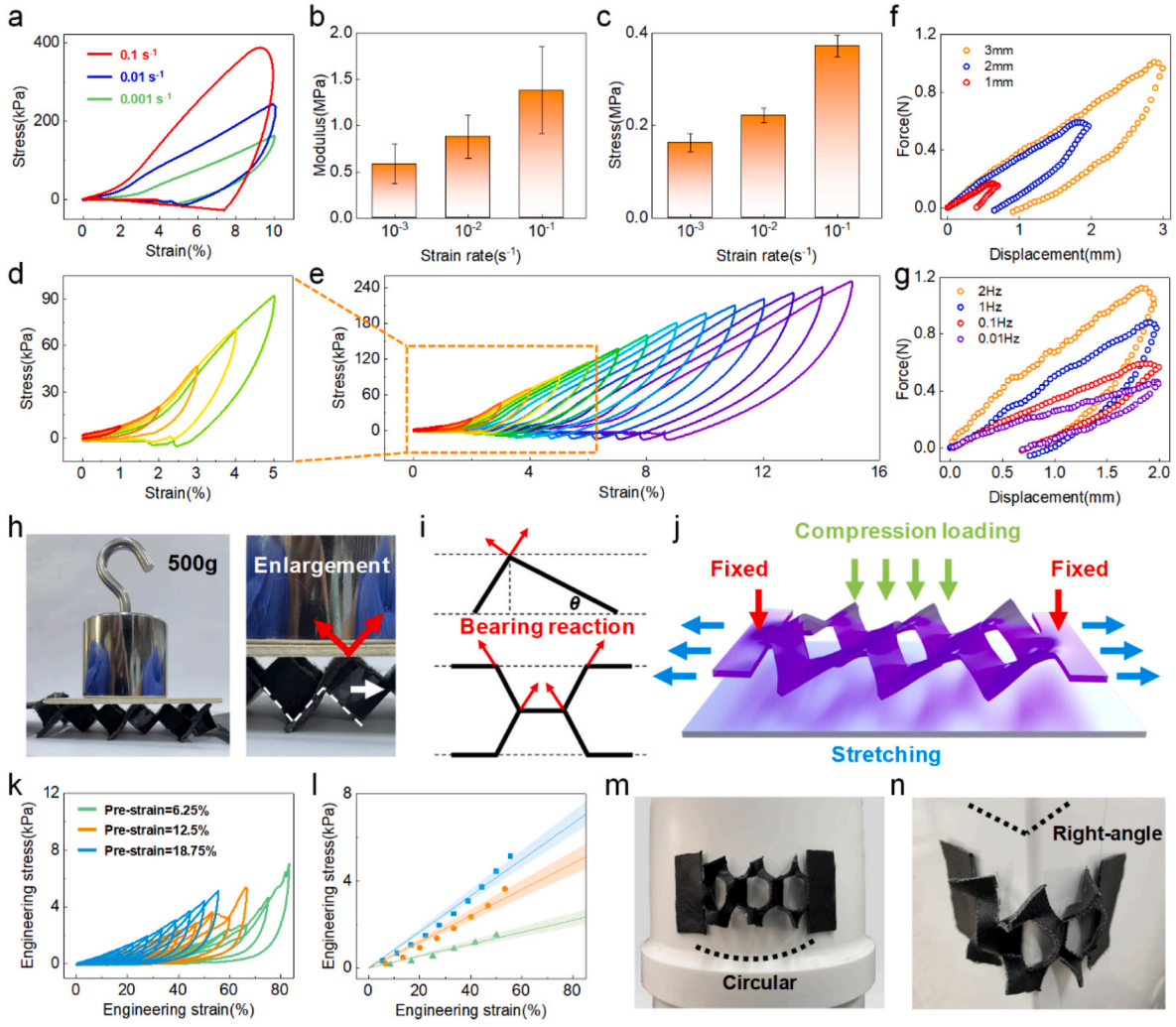

Fig. 4. (a) Typical compression stress–strain curves of structureless Kiri-Kevlar; statistics of (b) initial modulus and (c) maximum stress of compression under different strain rates; (d, e) compressive stress–strain curves of multiloading cycles, incrementally controlling the strain from 1% to 15%; three-point bending experiments for structureless Kiri-Kevlar under different (f) loading displacements and (g) frequencies; (h) load-carrying capacity of structured Kiri-Kevlar; (i) simplified feature area of structured Kiri-Kevlar; (j) schematic diagram of the boundary conditions for the compression test of structured Kiri-Kevlar; (k) engineering stress-engineering strain curve and (l) stiffness fitting of structured Kiri-Kevlar under compressive loading (0.01 mm/s); structured Kiri-Kevlar could attach well on (m) circular surfaces or (n) right angle areas.

unstructured Kiri-Kevlar samples with varying maximum strains. At a strain of 2%, a significant strengthening effect occurred (Fig. 4d). However, at higher strains, the stress–strain curve is found to be dependent on the historical maximum load, leading to the manifestation of the Mullins effect (Fig. 4e). A three-point bending experiment is conducted on unstructured Kiri-Kevlar. As the loading displacement increases, the support reaction also increases (Fig. 4f). Additionally, the Kiri-Kevlar also exhibits a clear shear thickening effect under the bending load (Fig. 4g). It is evident that structured Kiri-Kevlar, obtained via pre-strain, possesses an additional load-bearing capacity in comparison to unstructured Kiri-Kevlar, with the ability to even support up to 58.2 times its own weight (Fig. 4h). This additional load bearing capacity is mainly due to periodic truss structures (Fig. 4i), which are marked in the finite element model (Figure S23). The structural deformation of kirigami structure can be simplified to truss model. When the structured Kiri-Kevlar is subjected to external loads, it can provide stable bearing reaction force, which in the truss model is considered to be along the truss rod direction. To quantitatively evaluate the compression strength of the structured Kiri-Kevlar, a custom fixture is fabricated to secure the two ends of the Kiri-Kevlar and apply pre-strain by adjusting the distance (Figure S24a). Once structured, Kiri-Kevlar is subjected to vertical compression loading by the MTS system (Fig. 4j, Figure S24b). The deformation degree of structured Kiri-Kevlar varies depending on the magnitude of the pre-strain. Higher strains result in a greater degree of lateral expansion (as demonstrated in the previous section). Additionally, the larger structural rotation angle makes the component of the support reaction in the horizontal direction smaller, thus providing more efficient support. Cyclic compression loading of structured Kiri-Kevlar with varying degrees of pre-strain is conducted at different strain levels (Fig. 4k). The resulting extreme stress points are fitted linearly. It is found that Kiri-Kevlar with a more structured degree exhibits higher structural stiffness (Fig. 4l). Even when structured, the Kiri-Kevlar demonstrates a significant shear stiffening effect when subjected to compression. The higher strain rate and greater pre-strain synergistically enhance the load carrying capacity of the structured Kiri-Kevlar (Figure S25). It is noteworthy that when the pre-strain is 6.25%, the stress experiences a sharp increase under high compressive strain. This can be attributed to the fact that Kiri-Kevlar has been completely flattened and the structure could not be furtherly deformed. In addition to being suitable for flat areas, the structured Kiri-Kevlar can also be fitted to cylindrical or right-angle areas without damaging the structure (Fig. 4m and n), demonstrating its feasibility for wearing on curved body surfaces such as arms and hips. To verify the bearing capacity under curved surface of Kiri-Kevlar, a 3D printed model based on the dimensions of the human elbow joint is created. Kiri-Kevlar demonstrates effective load-bearing capabilities under bending conditions (Figure S26a). In contrast, neat Kevlar is prone to breaking under even slight loads due to its weak interface properties (Figure S26b).

3.5. *Interlayer interface performance and anti-impact property of Kiri-Kevlar*

Structured Kiri-Kevlar is specifically designed to provide impact resistance when worn on the human body. To ensure its robustness under impact loading, Kiri-Kevlar requires high interfacial properties between different composite components. For both neat Kevlar and Kiri-Kevlar, a yarn pull-out test is conducted (Figure S27). The typical fiber pull-out curve for neat Kevlar is illustrated in Fig. 5a. The poor interfacial properties between the fibers result in loosely woven fabric. C-SSE effectively enhances the interface properties of Kevlar fiber bundles by

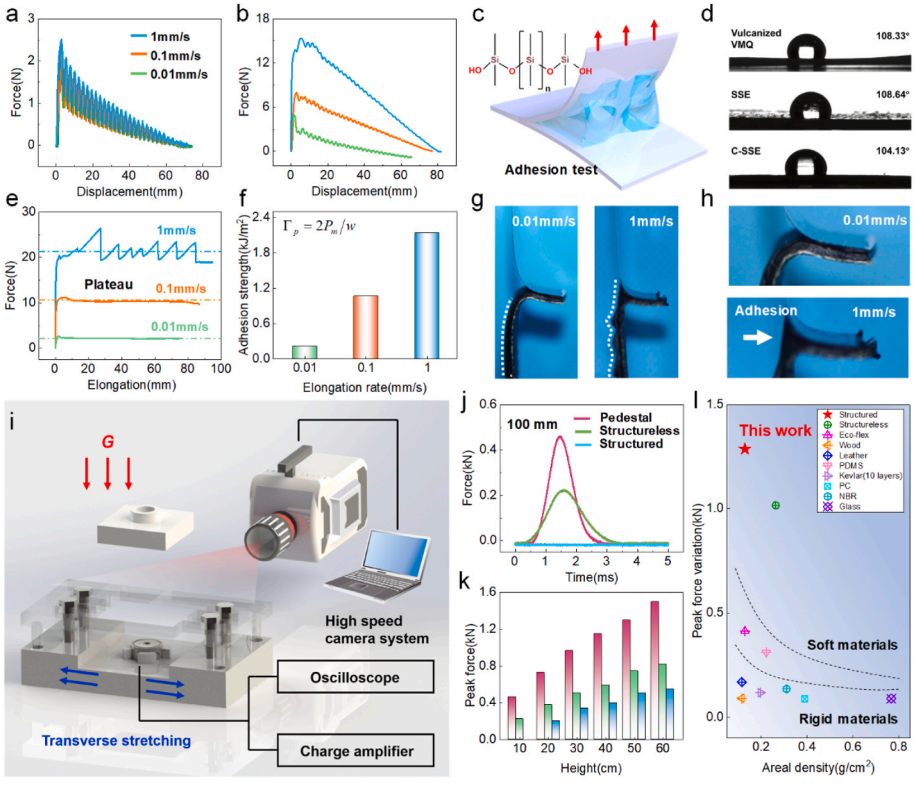

Fig. 5. Pull-out force vs. displacement curves for (a) neat Kevlar and (b) Kiri-Kevlar with different pulling rates; (c) schematic diagram of the T-peeling test for characterizing interface strength; (d) digital photos of water droplets in contact with vulcanized VMQ, SSE and c-SSE; (e) peeling force vs. extension curve and (f) adhesion strength statistics of Kiri-Kevlar with different strain rates; (g) interface morphology and (h) local magnification diagram during the T-peeling test; (i) schematic diagram of the low-velocity impact testing system; (j) typical force–time curves of pedestal, structureless/structured Kiri-Kevlar with impactor falling from 100 mm; (k) peak force statistics at different heights from 100 mm to 600 mm; (l) comparison of surface density and force dissipation of structured Kiri-Kevlar with a variety of different materials.

the shear stiffening effect (Fig. 5b). A hydrophilic surface possesses a higher surface free energy than a hydrophobic surface [39]. The surface of c-SSE contains a substantial number of hydrophilic groups (Si-OH), which contribute to its exceptional adhesion properties (Fig. 5c). The incorporation of carbon nanotubes (CNTs) has been demonstrated to enhance the mechanical strength of the matrix [40,41], thereby promoting interfacial bonding and further augmenting the hydrophilicity of the material (Fig. 5d). The adhesion strength between c-SSE and PET is characterized by a T-peeling test. The force–displacement curves of peeling at different strain rates are shown in Fig. 5e. The peeling force gradually reaches a plateau zone prior to the complete separation of the specimen. The adhesion strength (Γ_p) is defined as

$$\Gamma_p = 2P_m/w \tag{4}$$

where P_m is the average peeling force at the plateau and w is the width of the peeling specimen [42]. At a higher peeling velocity, the adhesion strength is significantly enhanced (Fig. 5f). The increase in adhesion strength leads to a notable variation in the morphology of the peeling surfaces (Fig. 5g, Figure S28). At a peeling velocity of 0.01 mm/s, c-SSE is stably removed from the PET, resulting in a relatively smooth surface (Video S5). However, at a peeling velocity of 1 mm/s, the peeling process becomes fluctuant, leading to the appearance of a wavy structure on the surface (Video S6). This is also reflected in the fluctuation of the platform region of the peeling curve, as shown in Fig. 5e. At a higher peeling velocity, there is a significant adhesion phenomenon in the peeling region, indicating a higher adhesion strength (Fig. 5h). When the removed PET and c-SSE are re-bonded by hand pressing, there is still a stable adhesion strength during the second peeling (Figure S29). To study the in-situ force dissipation ability of structured Kiri-Kevlar during impact loading, a test platform is set up, as shown in Fig. 5i. First, Kiri-Kevlar is structured by applying pre-strain. The impactor is released vertically, and a force sensor is placed underneath to measure the remaining force after being buffered. The entire impact process is recorded using a high-speed camera positioned on the side. When the falling height is 100 mm, the peak impact force without protection is 0.46 kN, and structured Kiri-Kevlar almost completely dissipates the impact force before the impactor contacts the force sensor (Fig. 5j–Video S7). The original impact force curves at different heights are presented in Figure S30. At higher heights, the shear stiffening effect of c-SSE and the stiffness of the Kiri-Kevlar structure play an excellent force dissipation role (Fig. 5k), which can also be proven by the extension of buffer time (Figure S31). In the composite structure of Kiri-Kevlar, conductive shear-stiffening elastomer plays a major role in impact force dissipation under low-speed impact loading. Low velocity impact experiments are also carried out on different material components of Kiri-Kevlar. Single-layer Kevlar fabric and single-layer PET are not present a significant

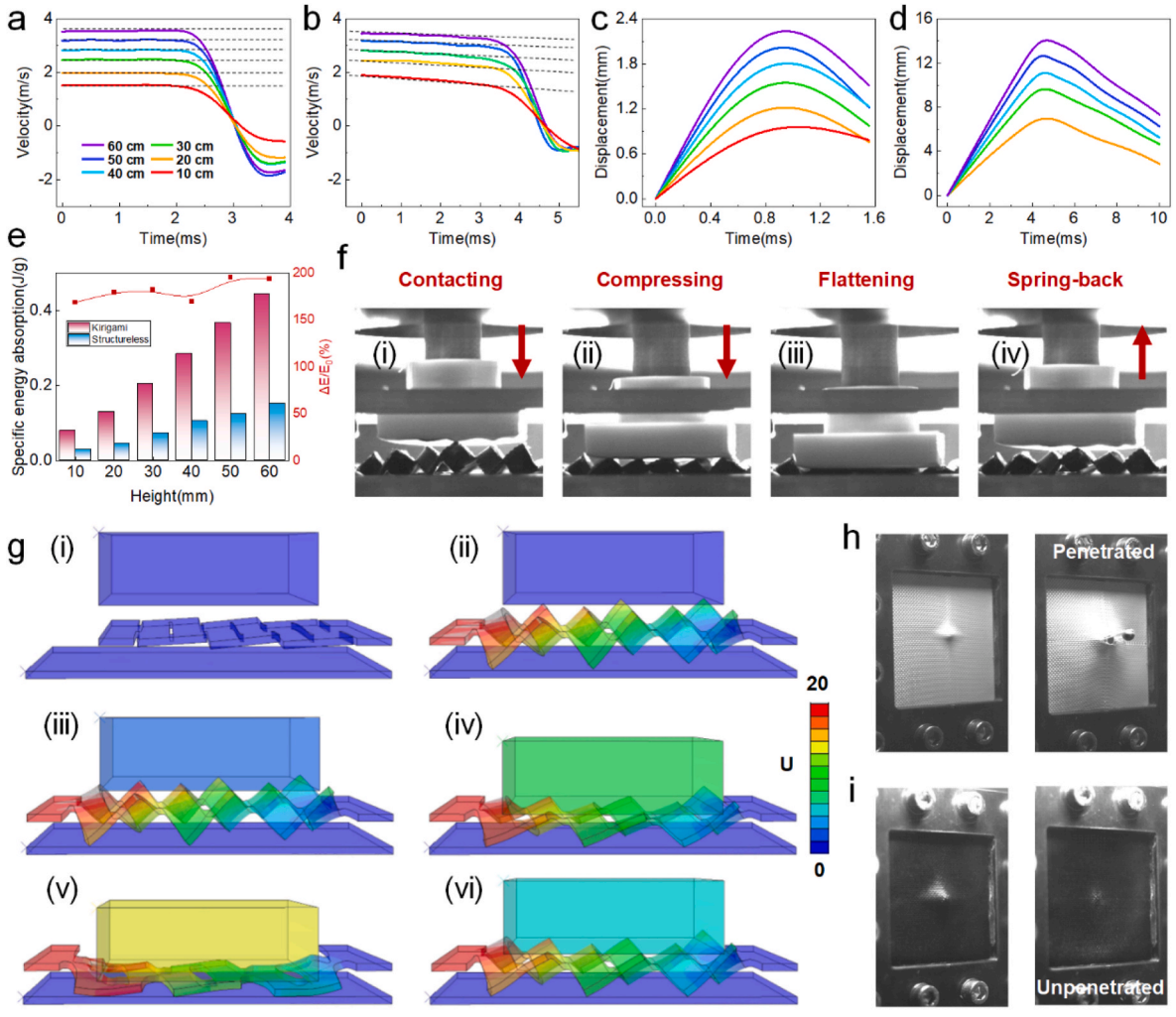

Fig. 6. Velocity vs. time of (a) structureless and (b) structured Kiri-Kevlar; displacement vs. time of (c) structureless and (d) structured Kiri-Kevlar; (e) comparison of energy absorption by structured/structureless Kiri-Kevlar during impact; (f) structural deformation evolution of structured Kiri-Kevlar at the moment of impact; (g) FEM results of displacement field of structural deformation under impact loading; (h) penetration process diagrams of (h) neat Kevlar and (i) Kiri-Kevlar with initial velocities of 86.8 m/s and 84.8 m/s.

impact-dissipating effect at low-speed impact, while force dissipation performance of Kiri-Kevlar is excellent (Figure S32). Furthermore, many common materials can be used as protective layers, and soft materials tend to have better force dissipation capacity than rigid materials without structure design due to high deformation capacity. In this work, the force dissipation capacity of structured Kiri-Kevlar is far better than those of commonly used materials (Fig. 5l–S33).

It is worth mentioning that c-SSE itself has impact resistance [43], and Kiri-Kevlar enhances this performance by structuring. Through the accelerometer installed on the impactor, the speed change during the impact can be calculated (Fig. 6a). Compared to the unstructured Kiri-Kevlar, the structured Kiri-Kevlar has more freedom under compression loading, and the speed starts to decline earlier (Fig. 6b). The displacement of the impactor can be obtained by Equation (5):

$$\Delta h = \int \left(\sqrt{2gh_0} - \int a \, \mathrm{dt} \right) \mathrm{dt} \tag{5}$$

where h_0, Δh, and a are the initial height, height variation during impact and accelerated speed of the impactor, respectively (Fig. 6c and d). The structure of Kiri-Kevlar incorporating periodic notches not only enhances energy dissipation but also reduces surface density, and there is a significant increase in energy dissipation per unit mass (Fig. 6e). This excellent energy dissipation ability comes from structural deformation. When the impactor contacts the structured Kiri-Kevlar [Fig. 6f (i)], the de-structuring process consumes part of the impact energy [Fig. 6f (ii)]. When Kiri-Kevlar is completely flattened, the shear stiffening effect from c-SSE further consumes energy [Fig. 6f (iii)]. Finally, the impactor bounces back, and the structure can also recover well [Fig. 6f (iv), Video S8]. By utilizing the displacement information recorded by the acceleration sensor on the impactor and high-speed camera system, the structural recovery at different heights are compared. For instance, when the impact speed is 100 mm, the non-resilient structure deformation of Kiri-Kevlar after impact is measured to be 1.3 mm, resulting in a resilience rate of 92.6%. As the impact height increases, the non-resilient structure deformation of Kiri-Kevlar gradually increases, leading to a decrease in the resilience rate. Upon reaching an impact height of 600 mm, the resilience rate is recorded as 59.3%. (Figure S34a). The process of applying pre-strain and subsequent impact can be more clearly demonstrated through an explicit dynamic model (Figure S34b). In the perspective model, the structured flattening and rebounding of Kiri-Kevlar during impact can be clearly observed (Fig. 6g). The distribution of Mises stress during the structured and impact loading process of Kiri-Kevlar is shown in Figure S35. Under the loading of in-plane tension, the tensile stress appears around the stress concentration point (Figure S35a-d). Interestingly, when structured Kiri-Kevlar is subjected to impact outside the plane, unloading behavior appears in some areas, showing negative stiffness characteristic that is conducive to overall energy dissipation (Figure S35e-f) [44–46]. As the structure flattens, more regions are coupled into the buffer region, and at this stage, the energy dissipation is further realized by the shear hardening effect (Figure S35g-h). Furthermore, Kiri-Kevlar presents excellent wear resistance, which guarantees its robustness during impact in practical use (Figure S36). The introduction of c-SSE gives Kiri-Kevlar without notches higher impact strength under high speed velocity loadings. At an average initial speed of 85 m/s, the neat Kevlar is easily penetrated (Fig. 6h–Video S9), while the Kiri-Kevlar without a notch can effectively withstand bullets (Fig. 6i–Video S10). At the initial speed of 140.8 m/s, Kiri-Kevlar without a notch is observed to be penetrated (Video S11).

3.6. Application design based on the electromechanical coupling performance of Kiri-Kevlar

The aforementioned study demonstrated the stable electrical properties of Kiri-Kevlar, along with the ability to exhibit resistance changes in response to applied strain. The potential of this electromechanical coupling in the development of wearable protective devices is explored. Under tensile loading (Fig. 7a), the maximum stress exhibits a nonlinear increase with respect to strain (Fig. 7b). Concurrently, the peak resistance of the material also demonstrates an increase with strain (Fig. 7c). Tensile loading is primarily executed during the structuring process, whereas Kevlar is predominantly subjected to compressive loading from external sources when being structured and exposed to impact (Fig. 7d). During the compression process, there is obvious strain strengthening, which is conducive to impact resistance (Fig. 7e). Under structured compression loading, the resistance changes more dramatically (Fig. 7f). Under tensile loading, the goodness of fit R^2 value of linear fitting is 0.994, and the sensitivity calculated by the slope of linear fitting is 23.5 kΩ/mm (Figure S37a). During the process of structured compression, more regions are involved in deformation, so the amplitude of resistance change is larger. The R^2 value of the linear fit is 0.981, and the sensitivity calculated based on the slope of the linear fit is higher, at 74.9 kΩ/mm (Figure S37b). Interestingly, due to periodic notches in the structure of Kiri-Kevlar itself, it is naturally segmented into multiple sensing regions and forms an array. Electrical properties vary when different short sides are used as electrodes (Figure S38). When the middle region of Kiri-Kevlar is bent, the resistance changes significantly (recorded by electrodes No. 3–4), while the resistance signal in the other regions does not change (recorded by electrodes No. 1–2 and No. 5–6) (Fig. 7g). Apparently, Kiri-Kevlar is designed to be worn on the human body and provide protection in a “subconscious” defensive posture (Fig. 7h). The bending behavior causes the Kiri-Kevlar to stretch, resulting in a 3D structure (Fig. 7i). This structural transformation leads to changes in resistance, which can be detected and analyzed by a computer system (Video S12). By analyzing the resistance signals from multiple channels, various defensive postures can be distinguished (Fig. 7j–Video S13). Specifically, in a voltage divided circuit, Kiri-Kevlar is connected in series with a fixed resistor. The voltage signal changes of Kiri-Kevlar are collected by the DAQ system. These signals are then transmitted to LabVIEW for processing, including the operation of games (Fig. 7k). As an example, Kiri-Kevlar can be used on both arms to control games, where throwing a left punch results in blue character punching and throwing a right punch results in red character punching (Fig. 7l, m, Video S14). Furthermore, based on stable electromechanical coupling performance, Kiri-Kevlar can be envisioned for integration into more complex wearable intelligent systems.

4. Conclusion

In this study, a hot-pressing process is employed to combine Kevlar, shear stiffening gel, and PET, resulting in flexible kirigami structures (Kiri-Kevlar). Kiri-Kevlar exhibits exceptional mechanical properties and the achieves the ability to switch between 2D and 3D states due to the introduction of periodic notches. When the human body faces external impact, the subconscious reaction causes individuals to curl up, among other actions. This instantaneous response effectively triggers the structural transformation of Kiri-Kevlar. FEM is employed to systematically investigate the structuring process. By adjusting the structural parameters, the initial stiffness and Poisson’s ratio of the Kiri-Kevlar can be designed accordingly. Similar to a pangolin spreading its scales, Kiri-Kevlar provides additional structural stiffness, offering excellent protection. When subjected to impact, the Kiri-Kevlar structure, in combination with shear stiffening effects, effectively dissipates the impact force. Specifically, at a height of 60 cm, the impact force is reduced from 1.24 kN to 0.54 kN. The impact process recorded by a high-speed camera demonstrates Kiri-Kevlar’s remarkable resilience. Furthermore, as a wearable device, Kiri-Kevlar not only provides effective protection but also exhibits electrical responsiveness under different loads. This electrical signal can be utilized for flexible control in computer games. In summary, Kiri-Kevlar represents an innovative design for impact protection in wearable devices. Its stable electrical performance also expands its potential applications in the field of

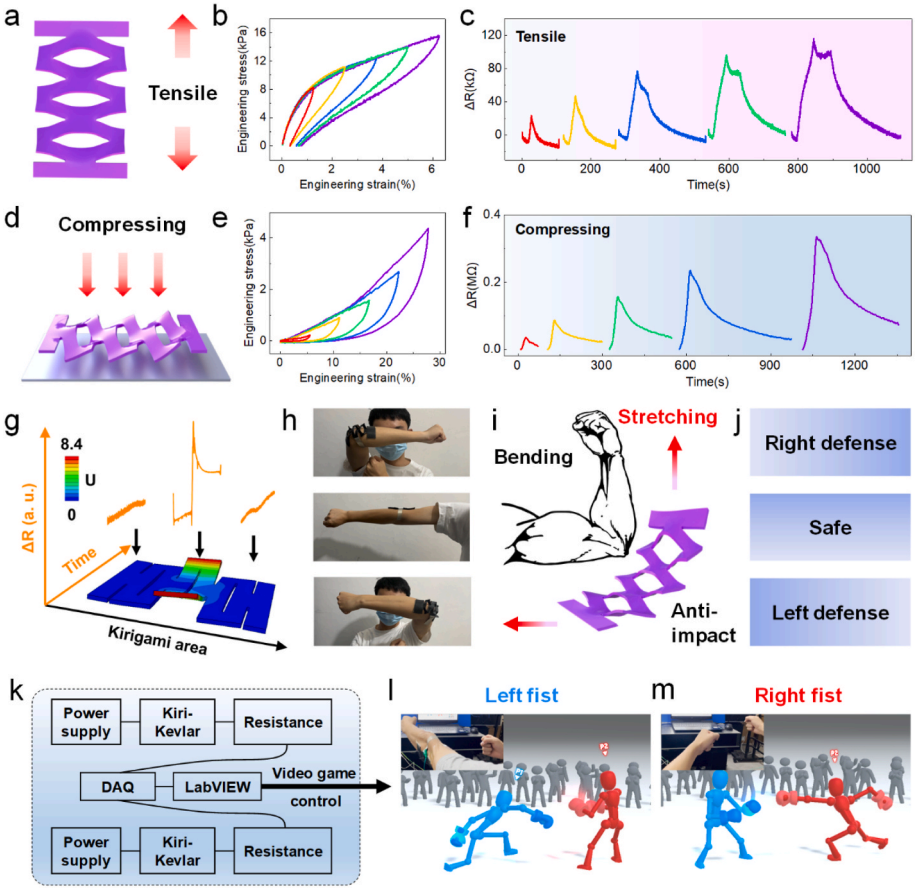

Fig. 7. (a) During cyclic tensile loading, (b) stable stress–strain curve and (c) response in situ resistance response; (d) during the cyclic compression process, (e) stable stress–strain curve and (f) response in situ resistance response of structured Kiri-Kevlar; (g) sensor array based on Kiri-Kevlar's intrinsical structure; (h) Kiri-Kevlar could be worn at the joints and (i) structured as arm bends, (j) taking on different defensive positions; (k) schematic diagram and working principle of real-time control computer system; (l, m) controlling computer game through different channels with Kiri-Kevlar.

human-computer interaction and holds great promise for future intelligent protective equipment.

CRediT authorship contribution statement

Jianyu Zhou: Writing – original draft, Visualization, Methodology, Investigation, Conceptualization. **Mei Liu:** Writing – original draft, Investigation, Formal analysis. **Sheng Wang:** Writing – review & editing, Validation, Methodology. **Junshuo Zhang:** Investigation, Formal analysis. **Mingyang Ni:** Writing – review & editing, Methodology. **Shuai Liu:** Formal analysis. **Yu Wang:** Visualization. **Huaxia Deng:** Visualization, Supervision. **Bing Liu:** Investigation, Formal analysis. **Xinglong Gong:** Supervision, Resources, Project administration, Funding acquisition.

Declaration of competing interest

The authors declare that they have no known competing financial interests or personal relationships that could have appeared to influence the work reported in this paper.

Data availability

Data will be made available on request.

Acknowledgements

Financial supports from the National Natural Science Foundation of China (Grant No. 12132016, 12172349, 52321003), USTC Research Funds of the Double First-Class Initiative (YD2480002004), and the Fundamental Research Funds for the Central Universities (Grant No. WK2480000010) were gratefully acknowledged. This study was also supported by the USTC Center for Micro and Nanoscale Research and Fabrication.

Appendix A. Supplementary data

Supplementary data to this article can be found online at https://doi.org/10.1016/j.compositesb.2024.111368.

References

[1] Bertoldi K, Vitelli V, Christensen J, Hecke M. Flexible mechanical metamaterials. Nat Rev Mater 2017;2:17066. https://doi.org/10.1038/natrevmats.2017.66.
[2] Dudte LH, Choi GPT, Becker KP, Mahadevan L. An additive framework for kirigami design. Nat Comput Sci 2023;3(5):443–54. https://doi.org/10.1038/s43588-023-00448-9.
[3] Blees MK, Barnard AW, Rose PA, Roberts SP, McGill KL, Huang PY, Ruyack AR, Kevek JW, Kobrin B, Muller DA, McEuen PL. Graphene kirigami. Nature 2015;524:204–7. https://doi.org/10.1038/nature14588.
[4] Zhang XN, Zheng Q, Wu ZL. Recent advances in 3D printing of tough hydrogels: a review. Compos B Eng 2022;238:109895. https://doi.org/10.1016/j.compositesb.2022.109895.
[5] Zhang H, Zhang M, Li J, Yang B, Abbas SC, Fu C, Chen T, Xia Y, Liu J, Du X, He Z, Ni Y. Aramid nanofiber-based functional composite materials: preparations, applications and perspectives. Compos B Eng 2024;271:111151. https://doi.org/10.1016/j.compositesb.2023.111151.
[6] Li X, Zhu P, Zhang S, Wang X, Luo X, Leng Z, Zhou H, Pan Z, Mao Y. A self-supporting, conductor-exposing, stretchable, ultrathin, and recyclable kirigami-structured liquid metal paper for multifunctional e-skin. ACS Nano 2022;16(4):5909–19. https://doi.org/10.1021/acsnano.1c11096.

[7] Zhou X, Ren L, Song Z, Li G, Zhang J, Li B, Wu Q, Li W, Ren L, Liu Q. Advances in 3D/4D printing of mechanical metamaterials: from manufacturing to applications. Compos B Eng 2023;254:110585. https://doi.org/10.1016/j.compositesb.2023.110585.

[8] Jang B, Won S, Kim J, Kim J, Oh M, Lee H, Kim J. Auxetic meta-display: stretchable display without image distortion. Adv Funct Mater 2022;32(22):2113299. https://doi.org/10.1002/adfm.202113299.

[9] Cheng Y, Lu H, Lee X, Zeng H, Priimagi A. Kirigami-based light-induced shape-morphing and locomotion. Adv Mater 2020;32(7):1906233. https://doi.org/10.1002/adma.201906233.

[10] Li H, Wang W, Yang Y, Wang Y, Li P, Huang J, Li J, Lu Y, Li Z, Wang Z, Fan B, Fang J, Song W. Kirigami-based highly stretchable thin film solar cells that are mechanically stable for more than 1000 cycles. ACS Nano 2020;14(2):1560–8. https://doi.org/10.1021/acsnano.9b06562.

[11] Listyawan MA, Song H, Jung JY, Shin J, Hwang G, Song HC, Ryu J. Magnetically driven powerless lighting device with kirigami structured magneto-mechanoluminescence composite. Adv Sci 2023;10(17):2207. https://doi.org/10.1002/advs.202207722.

[12] Li H, Wang Z, Sun M, Zhu H, Liu H, Tang CY, Xu L. Breathable and skin-conformal electronics with hybrid integration of microfabricated multifunctional sensors and kirigami-structured nanofibrous substrates. Adv Funct Mater 2022;32(32):2202792. https://doi.org/10.1002/adfm.202202792.

[13] Brooks AK, Chakravarty S, Ali M, Yadavalli VK. Kirigami-inspired biodesign for applications in healthcare. Adv Mater 2022;34(18):2109550. https://doi.org/10.1002/adfm.202202792. 10.1002/adma.202109550.

[14] Wang Z, Wang S, Du Z, Yang L, Cheng X, Wang H. Multifunctional wearable electronic textile based on fabric modified by MXene/Ag NWs for pressure sensing, EMI and personal thermal management. Compos B Eng 2023;266:110999. https://doi.org/10.1016/j.compositesb.2023.110999.

[15] Gao B, Elbaz A, He Z, Xie Z, Xu H, Liu S, Su E, Liu H, Gu Z. Bioinspired kirigami fish-based highly stretched wearable biosensor for human biochemical–physiological hybrid monitoring. Adv Mater Technol 2018;3(4):1700308. https://doi.org/10.1002/admt.201700308.

[16] Won P, Park JJ, Lee T, Ha I, Han S, Choi M, Lee J, Hong S, Cho K, Ko SH. Stretchable and transparent kirigami conductor of nanowire percolation network for electronic skin applications. Nano Lett 2019;19(9):6087–96. https://doi.org/10.1021/acs.nanolett.9b02014.

[17] Zhang Z, Qian L, Huang G, Chen C, Cheng J, Yao X, Ma C, Zhang G. Insertion of urea moieties for one-component strong yet tough, self-healing polyurea protective materials. Adv Funct Mater 2023;34(4):2310603. https://doi.org/10.1002/adfm.202310603.

[18] Zhang J, Wang Y, Deng H, Zhou J, Liu S, Wu J, Sang M, Gong X. A high anti-impact STF/Ecoflex composite structure with a sensing capacity for wearable design. Compos B Eng 2022;233:109656. https://doi.org/10.1016/j.compositesb.2022.109656.

[19] Zhou J, Zhang J, Sang M, Liu S, Yuan F, Wang S, Sun S, Gong X. Advanced functional Kevlar composite with excellent mechanical properties for thermal management and intelligent safeguarding. Chem Eng J 2022;428:131878. https://doi.org/10.1016/j.cej.2021.131878.

[20] Li S, Fang H, Sadeghi S, Bhovad P, Wan K. Architected origami materials: how folding creates sophisticated mechanical properties. Adv Mater 2019;31(5):180528. https://doi.org/10.1002/adma.201805282.

[21] Li Z, Chen W, Hao H, Yang Q, Fang R. Energy absorption of kirigami modified corrugated structure. Thin-Walled Struct 2020;154:106829. https://doi.org/10.1016/j.tws.2020.106829.

[22] Li Z, Yang Q, Chen W, Hao H, Matenga C, Huang Z, Fang R. Impact response of a novel sandwich structure with kirigami modified corrugated core. Int J Impact Eng 2021;156:103953. https://doi.org/10.1016/j.ijimpeng.2021.103953.

[23] Park C, Lee Y, Jang J, Han M. Origami and kirigami structure for impact energy absorption: its application to drone guards. Sensors 2023;23(4):2150. https://doi.org/10.3390/s23042150.

[24] Wang W, Wang S, Zhou J, Deng H, Sun S, Xue T, Ma Y, Gong Xinglong. Bio-inspired semi-active safeguarding design with enhanced impact resistance via shape memory effect. Adv Funct Mater 2023;33(13):2212093. https://doi.org/10.1002/adfm.202212093.

[25] Ma Y, Hong X, Xu Y, Lei Z, Huang G. Shear response behavior of SSE/Kevlar composite fabric before and after shear interlocking effect. Compos Struct 2023;314:116979. https://doi.org/10.1016/j.compstruct.2023.116979.

[26] Wang C, Lv Z, Mohan M, Cui Z, Liu Z, Jiang Y, Li J, Wang C, Pan S, Karim M, Liu AQ, Chen X. Pangolin-inspired stretchable, microwave-invisible metascale. Adv Mater 2021;33(41):2102. https://doi.org/10.1002/adma.202102131.

[27] Wang B, Yang W, Sherman VR, Meyers MA. Pangolin armor: overlapping, structure, and mechanical properties of the keratinous scales. Acta Biomater 2016;41:60–74. https://doi.org/10.1016/j.actbio.2016.05.028.

[28] Sang M, Liu S, Wu J, Wang X, Zhang J, Xu Y, Wang Y, Li J, Li J, Xuan S, Gong X. Flexible and breathable 3d porous SSE/MXene foam towards impact/electromagnetic interference/bacteria multiple protection performance for intelligent wearable devices. Nano Res 2023;16(7):10164–74. https://doi.org/10.1007/s12274-023-5523-3.

[29] Noury N, Poujaud J, Cousin P, Poujaud N. Biomechanical analysis of a fall: velocities at impact. IEEE Engineering in Medicine and Biology Society Conference Proceedings 2016:561–5. https://doi.org/10.1109/EMBC.2016.7590764.

[30] Meng L, Ceccarelli M, Yu Z, Chen X, Huang Q. An experimental characterization of human falling down. Mech Sci 2017;8(1):79–89. https://doi.org/10.5194/ms-8-79-2017.

[31] Sarvi MN, Luo Y. Sideways fall-induced impact force and its effect on hip fracture risk: a review. Osteoporos Int 2017;28(10):2759–80. https://doi.org/10.1007/s00198-017-4138-5.

[32] Farsadi M, Öchsner A, Rahmandoust M. Numerical investigation of composite materials reinforced with waved carbon nanotubes. J Compos Mater 2013;47(11):1425. https://doi.org/10.1177/0021998312448495.

[33] Boland CS, Khan U, Ryan G, Barwich S, Charifou R, Harvey A, Backes C, Li Z, Ferreira MS, Möbius ME, Young RJ, Coleman JN. Sensitive electromechanical sensors using viscoelastic graphene-polymer nanocomposites. Science 2016;354(6317):1257–60. https://doi.org/10.1126/science.aag2879.

[34] Boland CS, O'Driscoll DP, Kelly AG, Boland JB, Coleman JN. Highly sensitive composite foam bodily sensors based on the g-putty ink soaking procedure. ACS Appl Mater Interfaces 2021;13(50):60489–97. https://doi.org/10.1021/acsami.1c19950.

[35] O'Driscoll DP, McMahon S, Garcia J, Biccai S, Gabbett C, Kelly AG, Barwich S, Moebius M, Boland CS, Coleman JN. Printable g-putty for frequency- and rate-independent, high-performance strain sensors. Small 2021;17(23):2006542. https://doi.org/10.1002/smll.202006542.

[36] Haque ABMT, Hwang D, Bartlett MD. Graded Kirigami composites for programmed strain distributions. Adv Mater Technol 2022;7(7):2101241. https://doi.org/10.1002/admt.202101241.

[37] Lamoureux A, Lee K, Shlian M, Forrest SR, Shtein M. Dynamic kirigami structures for integrated solar tracking. Nat Commun 2015;6:8092. https://doi.org/10.1038/ncomms9092.

[38] Fan T, Sun Z, Zhang Y, Li Y, Chen Z, Huang P, Fu S. Novel Kevlar fabric composite for multifunctional soft body armor. Compos B Eng 2022;242:110106. https://doi.org/10.1016/j.compositesb.2022.110106.

[39] Liu J, Yao Y, Chen S, Li X, Zhang Z. A new nanoparticle-reinforced silicone rubber composite integrating high strength and strong adhesion. Compos Appl Sci Manuf 2021;151:106645. https://doi.org/10.1016/j.compositesa.2021.106645.

[40] Hyun BG, Jun Y, Lee J, Hamidinejad M, Saadatnia Z, Naguib HE, Park CB. Fabrication of microcellular TPU/BN-CNT nanocomposite foams for high-performance all-in-one structure triboelectric nanogenerators. Compos B Eng 2023;262:110813. https://doi.org/10.1016/j.compositesb.2023.110813.

[41] Ou Y, Wu L, Yi X, Mao D. Understanding Mode I interlaminar toughening of unidirectional CFRP laminates interleaved with aligned ultrathin CNT fiber veils: thickness and orientation effects. Compos B Eng 2023;254:110578. https://doi.org/10.1016/j.compositesb.2023.110578.

[42] Wang Z, Xiang C, Yao X, Floch PL, Mendez J, Suo Z. Stretchable materials of high toughness and low hysteresis. Proc Natl Acad Sci USA 2019;116(13):5967–72. https://doi.org/10.1073/pnas.1821420116.

[43] Zhou J, Wang S, Yuan F, Zhang J, Liu S, Zhao C, Wang Y, Gong X. Functional Kevlar-based triboelectric nanogenerator with impact energy-harvesting property for power source and personal safeguard. ACS Appl Mater Interfaces 2021;13(5):6575–84. https://doi.org/10.1021/acsami.0c18308.

[44] Sun M, Zhang K, Chen Y, Zhang Z, Chai H, Zhang G, Jiang S. Negative stiffness and buffering characteristics analysis of bistable laminates with initial curing curvature. Compos Struct 2023;308:116685. https://doi.org/10.1016/j.compstruct.2023.116685.

[45] Chen S, Liu X, Hu J, Wang B, Li M, Wang L, Zou Y, Wu L. Elastic architected mechanical metamaterials with negative stiffness effect for high energy dissipation and low frequency vibration suppression. Compos B Eng 2023;267:111053. https://doi.org/10.1016/j.compositesb.2023.111053.

[46] Jiang W, Ren X, Wang SL, Zhang XG, Zhang XY, Luo C, Xie YM, Scarpa F, Alderson A, Evans KE. Manufacturing, characteristics and applications of auxetic foams: a state-of-the-art review. Compos B Eng 2022;235:109733. https://doi.org/10.1016/j.compositesb.2022.109733.